Soft Tubular Strain Sensors for Contact Detection

Kevin Dai[1], Abirami Elangovan[1], Karen Whirley[1], and Victoria A. Webster-Wood[1,2,3(✉)]

[1] Department of Mechanical Engineering, Carnegie Mellon University, Pittsburgh, USA
vwebster@andrew.cmu.edu
[2] Department of Biomedical Engineering, Carnegie Mellon University, Pittsburgh, PA, USA
[3] McGowan Institute for Regenerative Medicine, Carnegie Mellon University, Pittsburgh, PA, USA

Abstract. Sensing and actuation are intricately connected in soft robotics, where contact may change actuator mechanics and robot behavior. To improve soft robotic control and performance, proprioception and contact sensors are needed to report robot state without altering actuation mechanics or introducing bulky, rigid components. For bioinspired McKibben-style fluidic actuators, prior work in sensing has focused on sensing the strain of the actuator by embedding sensors in the actuator bladder during fabrication, or by adhering sensors to the actuator surface after fabrication. However, material property mismatches between sensors and actuators can impede actuator performance, and many soft sensors available for use with fluidic actuators rely on costly or labor-intensive fabrication methods. Here, we demonstrate a low-cost and easy-to manufacture-tubular liquid metal strain sensor for use with soft actuators that can be used to detect actuator strain and contact between the actuator and external objects. The sensor is flexible, can be fabricated with commercial-off-the-shelf components, and can be easily integrated with existing soft actuators to supplement sensing, regardless of actuator shape or size. Furthermore, the soft tubular strain sensor exhibits low hysteresis and high sensitivity. The approach presented in this work provides a low-cost, soft sensing solution for broad application in soft robotics.

Keywords: Soft robotics · Strain sensor · Contact detection

This work was supported by NSF DBI2015317 as part of the NSF/CIHR/DFG/FRQ/UKRI-MRC Next Generation Networks for Neuroscience Program and by the NSF Research Fellowship Program under Grant No. DGE1745016. Any opinions, findings, and conclusions or recommendations expressed in this material are those of the authors and do not necessarily reflect the views of the National Science Foundation.

F. Meder et al. (Eds.): Living Machines 2023, LNAI 14157, pp. 197–215, 2023.
https://doi.org/10.1007/978-3-031-38857-6_16

1 Introduction

Sensing and actuation are critical to enabling robots to interact with their environments. Actuators are used for locomotion, manipulation of external objects, and modification of the robot's internal state or configuration. Sensors can close the loop for robotic control by providing feedback about the environment or the robot's internal state. While significant research has gone into developing sensors and actuators for traditionally rigid robots, the field of soft, bioinspired robots has received less attention in developing sensorized actuators. Soft, bioinspired robots must deal with additional design constraints over their rigid counterparts due to using flexible materials, which can preclude the usage of many existing actuators and sensors [4,11]. Examples of actuators that have been developed to meet the needs of soft robotics include fluidic artificial muscles [15], dielectric actuators [7], and shape-memory alloys and polymers [5].

Of the available soft actuators, fluidic artificial muscles, such as the McKibben actuator, provide an accessible and well-characterized solution for soft robotic actuation. Fluidic artificial muscles demonstrate high power densities and can be easily manufactured at a low cost using commercially available components, without the need for specialized tooling [15]. These fluidic actuators are typically composed of an elastomer, such as a latex balloon, and selectively stiffened reinforcement, such as a braided mesh, that constrains the inflation of the elastomer when pressurized [9,10]. Sensors have been designed for integration with McKibben actuators and other fluidic artificial muscles by embedding resistive or capacitive sensing elements within the actuator's elastomer [6,8,16] or by mounting to the actuator's external surface [17]. However, these sensors are primarily intended to measure the length of the actuator. They may not provide additional sensing functionality, such as detecting contact along the actuator's length, which could be helpful for robotic manipulation. Furthermore, these sensors may suffer from complex fabrication methods or large form factors that limit their usage as soft robots utilize higher numbers of sensorized actuators. For creating accessible soft robots for applications such as grasping, where multiple fluidic actuators may be assembled together in close proximity [3], sensors with small form factors and facile integration with actuators are needed.

An ideal sensor not only requires a small form factor and easy integration with different actuators without affecting actuation, but also needs to be easy to manufacture. Since a common mode of failure in fluidic artificial muscles is due to fatigue failure of the elastomer [9], sensors should also accommodate the replacement or repair of elastomeric components, which may preclude the integration of sensors within the elastomer. Compact and easy-to-manufacture strain sensors can be formed by filling commercially available elastomer tubing with conductive fluids for either resistive or capacitive sensing [2,14,18], without requiring dedicated tooling. Such a sensor could then be wrapped around a McKibben actuator for detecting actuator strain or external contact, while enabling the facile repair of the actuator's elastomer components. For tubular sensors to be most effective, they should have a high fill volume with minimal air gaps within the tube and high connectivity between the internal conductive fluid

and external electrical connections. However, sealing the ends of these tubular sensors during the manufacturing process can be challenging, resulting in either large air gaps within the liquid or in fluid leakage when inserting solid conductive leads into the ends of the sensor. Additionally, existing tubular sensors reported in the literature require each sensor to be manufactured individually, which is time-consuming and increases production costs.

In this paper, we present a novel manufacturing technique that enables the rapid sequential manufacturing of multiple tubular strain gauges without significant fluid leakage by using hollow syringe needles to serve as conductive leads. We characterize the tubular strain gauge's resistive response and hysteresis. In addition, we demonstrate the capability of a helically-wound tubular strain gauge to detect contact during grasping with a toroidally-shaped McKibben actuator. As these sensors are low-cost, easy-to-manufacture, and easily mountable to a wide array of actuators, they have far-reaching potential in soft robotics by providing proprioception for internal state estimation and contact detection. These capabilities will enable sensorized actuators to enhance soft robotic performance in applications such as grasping, manipulating, and exploring external environments.

2 Methods

The presented tubular strain gauge uses a novel manufacturing method that enables the rapid sequential production of multiple sensors while maintaining a low part count. The strain gauge is fabricated by filling elastomer tubing with a conductive fluid, eutectic gallium-indium (EGaIn). Strain sensors of two different lengths were fabricated and characterized to acquire their resistance-strain response and mechanical stress-strain hysteresis response. In addition, one specimen of the longer strain sensor was attached to a McKibben actuator for evaluating both electromechanical hysteresis and contact detection.

2.1 Sensor Design and Fabrication

The strain gauge has a simple design with few components. In brief, hollow elastomer tubing is filled with an electrically-conductive fluid, EGaIn, to form a flexible, resistive wire. Crimped, conductive hypodermic needles are located at each end of the elastomer tubing and provide a solid, conducting surface for external electrical connections. Heat-shrink tubing and silicone adhesive are used to secure the stainless steel needles to the silicone tubing while preventing leakage of the internal conductive fluid.

Sensors were fabricated with lengths of 114.3 mm and 495.3 mm. To fabricate the sensors, silicone tubing (0.51 mm ID $\times$ 0.94 mm OD, Shore 55A, McMaster-Carr) was first cut to the desired length. We prepared 30.2 mm lengths of hypodermic tubing by applying a heat gun to nominally 25.4 mm-long, blunt 23G Luer-lock syringe needles while manually twisting the stainless steel tubing out of the plastic needle housing. A sharp blade was used to scrape away excess

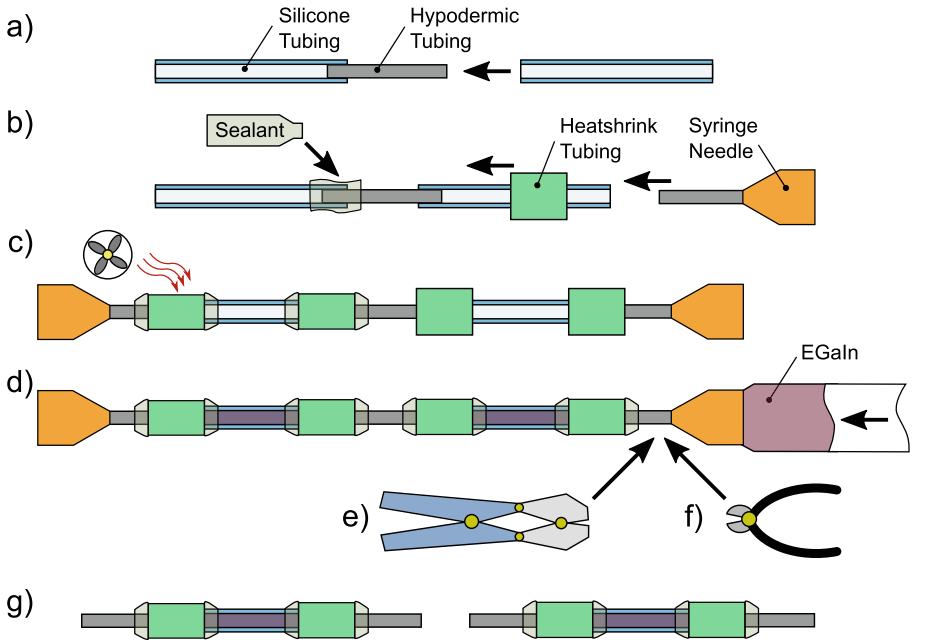

Fig. 1. The strain gauge presented in this work is simple to construct with a low part count. The sensors consisted of a conductive fluid inside an elastomer tube. a) For the construction of the strain gauge, conductive hypodermic tubing was first inserted into sections of silicone tubing that formed the body of the strain gauge. The hollow conductive tubing enabled the rapid manufacturing of multiple sensors in series. b) Sealant and heat shrink were applied to seal the joints between the hypodermic and elastomer tubing. Luer-lock syringe needles were inserted into the ends of the chain of tubes for later connection to a syringe. c) Excess sealant squeezed out after heat was applied to the heat-shrink tubing. The sealant was smoothed into a taper for a gradual transition in rigidity between the joint and the flexible, elastomer tubing. d) A conductive fluid, EGaIn, was injected into the chain of tubing until it reached the opposite end of the chain. e) Each length of the elastomer tubing was sealed from its neighbors in sequence by using a crimping tool on the hypodermic tubing. f) A cutting tool was used to pierce the crimped region of hypodermic tubing and to separate the EGaIn-filled tubes into distinct strain gauges. g) Additional crimping was performed on the ends of the hypodermic tubing for further sealing or on ferrules to attach wires to the ends of the strain gauge.

adhesive that remained on the outside surface of the hypodermic tubing after removal from the plastic needle housing.

Multiple lengths of silicone tubing could be chained together using hypodermic tubing for rapid sequential fabrication, with each length of silicone tubing forming a separate strain gauge (Fig. 1). Stainless steel hypodermic tubing was inserted with 6.4 mm of overlap into silicone tubing to form chains (Fig. 1a). Room-temperature-vulcanizing silicone sealant (Sil-Poxy, SmoothOn)

was applied evenly to the external surfaces of overlapping hypodermic and silicone tubing (Fig. 1b). To mechanically secure the joints between hypodermic and silicone tubing, 12.7 mm-lengths of 1.6 mm-diameter heat-shrink tubing were immediately placed over the uncured sealant at each joint and briefly heated with a heat gun until shrunk (Fig. 1c). Any uncured sealant that squeezed out from underneath the heat-shrink during heating was manually formed into a smooth taper for a gradual transition in stiffness near each joint while taking care to leave a central portion of hypodermic tubing exposed for future electrical connection (Fig. 1 c). 23G Luer-lock syringe needles were inserted into the silicone tubing at either end of the chain and similarly sealed (Fig. 1b-d).

After the sealant had cured, liquid metal EGaIn was drawn into a syringe and injected into one of the Luer-lock needles until reaching the opposite end of the tubing chain (Fig. 1d). Then, approximately 5 mm at the center of each exposed hypodermic tube was crimped flat using a compound-action crimping tool, beginning with the syringe needle and proceeding in sequence to the opposite end of the tubing chain (Fig. 1e). The crimped regions of hypodermic tubing were cut using diagonal cutting pliers to separate the tubing chain into individual strain gauges (Fig. 1f). After separating the sensors, approximately 2 mm of hypodermic tubing at the ends of each strain gauge were re-crimped for improved sealing and then served as electrical leads (Fig. 1g). For connection to a sensor amplifier circuit, the leads of each strain gauge were attached to lengths of copper wire (24 AWG) using crimped stainless steel ferrules.

2.2 Sensor Characterization

Strain gauges were characterized by evaluating their change in resistance with respect to strain, measuring their mechanical hysteresis on a tensile testing machine, and estimating their electromechanical hysteresis when mounted on a soft actuator.

Resistance-Strain Response. Each sensor's change in resistance was measured with respect to strain by connecting the strain gauge to an LCR meter (Atrix MCR-5030) and manually extending the strain gauge. Shorter, 114.3 mm-long strain gauges were extended in increments of 10 mm up to 200 mm, corresponding to a strain of 175%. Longer, 495.3 mm-long strain gauges were extended in increments of 10 mm up to 350 mm, corresponding to a strain of 71%.

The theoretical resistance of the strain gauges was calculated while assuming a constant volume of conductive fluid [8]:

$$V_F = A_0 L_0 = AL \tag{1}$$

$$R = \frac{\rho L}{A} \tag{2}$$

$$R = \frac{LA_0}{L_0 A} R_0 = \frac{L^2}{{L_0}^2} R_0 = (1+\varepsilon)^2 R_0 \tag{3}$$

where V_F is the volume of conductive fluid, A_0 and A are the initial and instantaneous fluid cross-section area (respectively), L_0 and L are the initial and instantaneous length of fluid (respectively), R_0 and R are the strain gauge's initial and instantaneous electrical resistance (respectively), ρ is the fluid's electrical resistivity, and ε is strain.

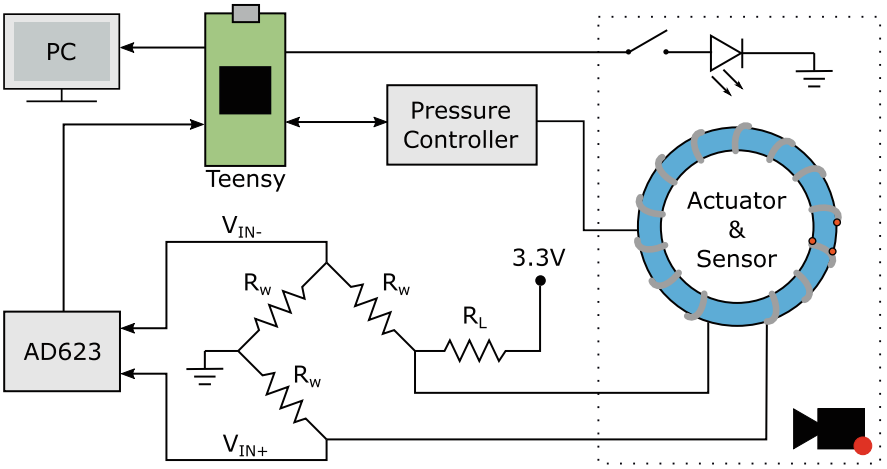

Fig. 2. Data logging setup for capturing the sensor signal from the strain gauge (thin grey lines), which is helically wrapped around a toroidal McKibben actuator (blue ring) during a test for electromechanical hysteresis. The strain gauge was connected to an amplified (AD623) Wheatstone bridge, and the amplified signal was recorded to a computer through a Teensy 4.0 microcontroller. A pressure controller received pressure setpoint values from the microcontroller and regulated the pressure in the McKibben actuator. The dotted rectangle indicates the region that was recorded by a video camera during hysteresis tests with a McKibben-mounted strain gauge. A manually-toggled switch and LED enabled synchronization between the video footage and the sensor data. Three fiducial markings on the actuator are used for tracking actuator strain in the video footage (orange dots). For mechanical hysteresis tests with the material testing system, the McKibben actuator and pressure controller are excluded from the data logging setup.

Mechanical Hysteresis. We evaluated the mechanical hysteresis of one 114.3 mm-long strain gauge and one 495.3 mm-long strain gauge in a material testing system (MTS Criterion Model 42, 50 N-load cell).

For the shorter 114.3 mm-long strain gauge, the crimped ends of the strain gauge were clamped by the testing system's fixed clamp and moving crosshead clamp. The maximum experimental crosshead extension was set to 114.3 mm, corresponding to 100% strain. For the longer 495.3 mm-long strain gauges, the testing system's maximum supported crosshead extension was insufficient to use

Table 1. Signal amplifier parameters for two different strain gauge lengths. The amplified Wheatstone bridge is shown in Fig. 2.

Parameter	Short Sensor	Long Sensor
Length (mm)	114.3	495.3
R_L (Ω)	$220 \pm 1\%$	$220 \pm 1\%$
R_W(Ω)	$1.0 \pm 1\%$	$1.62 \pm 1\%$
AD623 R_G (Ω)	$280 \pm 1\%$	$402 \pm 1\%$
AD623 Nominal Gain	358	250

the same clamping scheme as the shorter strain gauge. Instead, the 495.3 mm-long strain gauge was folded in half into an inverted U-shape that was 247.7 mm long. Both crimped ends were mounted in the testing system's fixed clamp, while the middle of the strain gauge was wrapped around a 10 mm-diameter disc magnet that was held in the moving crosshead clamp. The maximum experimental crosshead extension of the folded strain gauge was set to 247.7 mm, corresponding to a strain of 100%.

For both lengths of strain gauges, the MTS test program was set to sinusoidally cycle the strain gauges between 0% and 100% strain at 4 frequencies (0.25 Hz, 0.13 Hz, 0.063 Hz, and 0.031 Hz). Strain gauges were cycled for 4.5 periods within each frequency before proceeding to the next halved frequency. The crosshead returned to the position of 0 mm extension between frequencies. Load and extension data was logged to a text file at 100 Hz.

Electromechanical Hysteresis. To evaluate the sensor's electromechanical hysteresis in an applied setting, a strain gauge was mounted onto a McKibben actuator that was pressure cycled at multiple frequencies.

A toroidal McKibben actuator with a ∼100 mm major diameter was fabricated using methods described by Dai et al. [3]. In brief, a latex balloon was cut to a length of ∼280 mm and stretched over barbed reducer fittings (3.2 mm to 1.6 mm) at both ends. Braided mesh (9.5 mm, Flexo PET) was then pulled over the latex balloon and mechanically secured using a combination of Kevlar thread and cyanoacrylate adhesive. A 1.6 mm barbed T-fitting and two ∼12 mm-long pieces of polyethylene tubing (1.6 mm ID × 3.2 mm OD, McMaster-Carr) were used to form the actuator into a toroid.

A 495.3 mm-long strain gauge was helically wrapped around the uninflated McKibben actuator, forming 13 complete turns around the toroid's cross-section and reaching from one of the actuator's barbed fittings to the other (Fig. 2). Spots of silicone adhesive were applied to tack together the strain gauge and the actuator at the barbed fittings and 12 additional, periodically spaced locations along the outer circumference of the toroid.

To record the analog electrical signal from the strain gauge, the strain gauge was plugged into an amplified Wheatstone bridge (AD623) with 24 AWG wire (Fig. 2). The amplified signal was then read by a microcontroller (Teensy 4.0)

through an onboard 10-bit analog-to-digital converter (ADC) at a sampling frequency of 100 Hz and recorded to a text file on a PC through serial communication (PuTTY 0.70, 115200 Hz baud rate). Resistors for the Wheatstone bridge and amplifier gain were selected to prevent amplifier saturation at 100% strain (Table 1). The AD623 amplifier was setup with $+V_S = 3.3\,\text{V}$, $-V_S = 0\,\text{V}$, and $V_{REF} = +V_S/2 = 1.65\,\text{V}$ [1].

The Teensy microcontroller also controlled the pressure in the McKibben actuator through a pressure controller described in Dai et al. 2022 [3] while simultaneously logging the actuator's internal pressure signal (ELVH-030G-HAND-C-PSA4) to the same text file as the amplified strain gauge signal. The pressure controller received a sinusoidal pressure setpoint signal ranging from 0 to 69 kPa at 7 frequencies (1 Hz, 0.5 Hz, 0.25 Hz, 0.13 Hz, 0.063 Hz, 0.031 Hz, and 0.016 Hz). The actuator was cycled for 5 periods within each frequency before proceeding to the next halved frequency.

For calculating electromechanical hysteresis, the actuator's strain was estimated using computer vision to compare against the strain gauge's electrical signal. Video footage of the actuator and integrated strain gauge was recorded from a top-down view with the actuator resting on a tabletop surface (Canon EOS Rebel T7, 720p@60 Hz). For synchronizing the video footage and the microcontroller's data log, a button and LED were attached to the microcontroller and included in the frame of the video. By pushing the button, a Boolean flag was toggled in the data log and the LED simultaneously toggled on or off for reference in the video. The video's framerate of 60 Hz implies a maximum synchronization error of 16 ms. High-contrast, fiducial markings were created on the outside of the actuator using oil-based paint markers for easier tracking of actuator strain. The position data of three fiducial markings were tracked using Tracker 6.1.2 (Physlets) for estimating the toroidal actuator's strain along both the circumference and cross-sectional thickness.

Post-Processing Data Electromechanical hysteresis was evaluated by determining the relationship between strain measured by the video footage and strain measured by the strain gauge. Several data post-processing assumptions were made to determine the strain-strain relationship.

For the strain gauge, an empirically-derived relationship was used to convert between the amplified sensor voltage and strain values. The empirical relationship combined theoretically-derived output voltages from the amplified Wheatstone bridge, a theoretical relationship between strain and change in strain gauge resistance, and the experimentally-measured initial resistance of the strain gauge:

$$V_\varepsilon = G\left[\frac{R_W(R_W - R_\varepsilon)}{2R_W(R_W + R_\varepsilon) + R_L(3R_W + R_\varepsilon))}\right]V_P + V_{REF} \tag{4}$$

$$\%\Delta R = \frac{R_\varepsilon}{R_0} - 1 = \frac{(1+\varepsilon)^2 R_0}{R_0} - 1 = \varepsilon^2 + 2\varepsilon \tag{5}$$

where V_ε is the amplified sensor voltage, G is the AD623 amplifier's gain, R_W is the resistance of Wheatstone bridge resistors (Fig. 2), R_ε is the strain gauge

resistance, R_L is the resistance of an inline resistor to the Wheatstone bridge, $V_P = 3.3V$ is the voltage applied to the inline resistor, and $V_{REF} = 1.65V$ is the amplifier's reference voltage.

For the video footage, numerous assumptions were made to estimate the strain experienced by the strain gauge. Since the strain gauge was wrapped helically around the McKibben actuator, the strain gauge experienced a combination of strains from the expansion of the actuator's balloon cross-section as well as the contraction of the toroid circumference. The standard length of a helix can be calculated using:

$$L_H = n\sqrt{(p^2 + C^2)} \tag{6}$$

where L_H is the length of the helix, n is the number of turns, p is the helical pitch, and C is the helix's circumference.

From the three tracked points on the inner and outer diameter of the toroidal actuator (Fig. 2, orange dots), we calculated the pitch of the strain gauge helix as well as the cross-section thickness of the McKibben actuator.

The McKibben actuator's cross-section shape changes with inflation pressure (Fig. 3). At low pressures, the cross-section narrows due to the flatness of the actuator's braided mesh. As the actuator inflates, the cross-section becomes more circular. Therefore, we calculated the perimeter of the cross-section as a substitute for the helical circumference, C. We modeled the cross-section geometry using two circular arcs. The sum of arc lengths was equal to the perimeter of the helix. Arc lengths were calculated by finding the center point of the arc, then calculating the radius of the arc and the arc's central angle.

We placed the origin of our coordinate system at the center of the two circular arcs (Fig. 3a,b, white arrows). To find the center point of one of the circular arcs, we identified three points along the arc and applied the equation of a circle:

$$\begin{bmatrix} x_1 & y_1 \\ x_2 & y_2 \\ x_3 & y_3 \end{bmatrix} = \begin{bmatrix} 0 & \frac{h}{2} \\ \frac{t}{2} & 0 \\ 0 & -\frac{h}{2} \end{bmatrix} \tag{7}$$

$$r^2 = (x - x_C)^2 + (y - y_C)^2 \tag{8}$$

$$\begin{bmatrix} 2(x_1 - x_3) & 2(y_1 - y_3) \\ 2(x_1 - x_2) & 2(y_1 - y_2) \end{bmatrix} \begin{bmatrix} x_C \\ y_C \end{bmatrix} = \begin{bmatrix} x_1^2 - x_3^2 + y_1^2 - y_3^2 \\ x_1^2 - x_2^2 + y_1^2 - y_2^2 \end{bmatrix} \tag{9}$$

where h is the height of the actuator's cross-section, t is the thickness of the actuator's cross-section, r is the radius of the circular arc, and (x_C, y_C) is the center point of the arc. Then, the arc length and the actuator's cross-sectional perimeter were calculated:

$$s = r\theta \tag{10}$$

$$\theta = 2\arctan\left(\frac{y_1 - y_C}{x_1 - x_C}\right) \tag{11}$$

$$C = 2s \tag{12}$$

where s is the arc length, θ is the central angle, and C is the circumference or perimeter of the actuator's cross-section.

We measured thickness values, t, from the video footage and determined the height, h, using an empirically-derived relationship between t and h. To develop the empirical relationship between t and h, the actuator was inflated from 0 to 69 kPa in increments of 6.9 kPa, while t and h were measured manually using calipers. Then we fit a second-order curve to the data assuming units in millimeters (Fig. 3c):

$$h = 0.033t^2 - 0.367t + 15.7 \tag{13}$$

Near the actuator's fittings, the cross-section was constrained by the barbed fitting to be more circular. To estimate the strain gauge's strain near the barbed fittings, we applied another assumption that the cross-section geometry transitioned from a circular shape at the barbed fitting to the actuator's standard cross-section within the span of half a turn of the strain gauge's helix. For a full turn, the length of the strain gauge near the fittings was estimated by:

$$L_E = \sqrt{p^2 + \left(\frac{3C + \pi d}{4}\right)^2} \tag{14}$$

where L_E is the length of the strain gauge helix at the conical ends of the actuator and $d = 10$ mm is the fixed diameter of the actuator cross-section near the barbed fitting.

The full length of the strain gauge, with 11 standard turns and 2 conical end turns, was calculated by combining Eqs. 6 and 14:

$$L_\varepsilon = 11L_H + 2L_E \tag{15}$$

where L_ε is the full length of the strain gauge when wrapped around the actuator. This enabled us to estimate the strain seen by the strain sensor.

2.3 Contact Detection

To explore the contact detection capabilities of the strain sensor, we pressurized the toroidal McKibben actuator and monitored the strain gauge signal before and after placing a tennis ball (Penn) within the circumference of the actuator. The same experimental setup was used as with electromechanical hysteresis testing. First, the actuator's pressure controller received a sinusoidal control signal for 5 cycles between 0 to 69 kPa at 0.13 Hz while no objects were present within the actuator's circumference, to serve as contactless reference data. Next, a tennis ball was placed within the actuator's circumference. The actuator was cycled again for 5 cycles between 0 to 69 kPa at 0.13 Hz to collect contact detection data.

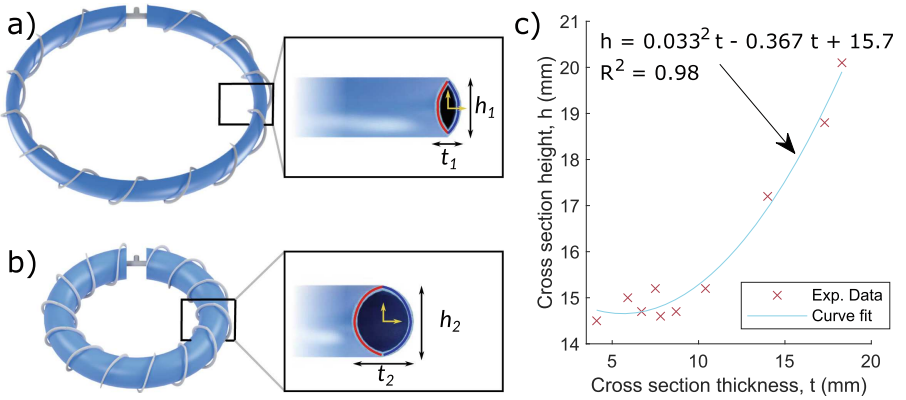

Fig. 3. The cross-section of the McKibben actuator changes shape depending on inflation pressure. a) At low pressure, the actuator's cross-section flattens, while b) at high pressure, the actuator's cross-section becomes more circular. The perimeter of the cross-section is modeled with two circular arcs (highlighted in red and blue). The coordinate system is represented by the white arrows. c) An empirical relationship between t and h was established by fitting a second-order curve to experimental data. This relationship was used to approximate the actuator height from thickness data taken from video footage of the actuator.

3 Results

3.1 Strain and Resistance

The experimental resistance-strain responses of three 495.3 mm-long strain gauges and two 114.3 mm-long strain gauges were found to be similar when compared to their theoretical quadratic responses (Fig. 4). Due to different starting resistances, R_0, for different lengths of strain sensors, we normalized the data to show % change in resistance. Second-order curves fit to the 495.3 mm-long strain gauge data and the 114.3 mm-long strain gauge data have R^2 values of 0.992 and 0.998, respectively. Both fitted curves lie below the theoretical resistance-strain relationship (Eq. 5), with the "Long" sensor data located closer to the theoretical curve than the "Short" sensor data.

3.2 Mechanical Hysteresis

Both tested lengths of strain gauges exhibited mechanical stress-strain hysteresis when loaded cyclically (Fig. 5a), with softening at intermediate strain values. Data were post-processed with an exponential moving average ($w = 10$). Only 1 out of every 15 markers was plotted for clarity. At a cycling frequency of 0.031 Hz, the 114.3 mm-long sensor exhibited a higher peak stress of 713 kPa at 98.2% strain, compared to the 495.3 mm-long sensor's peak stress of 592 kPa at 98.2% strain.

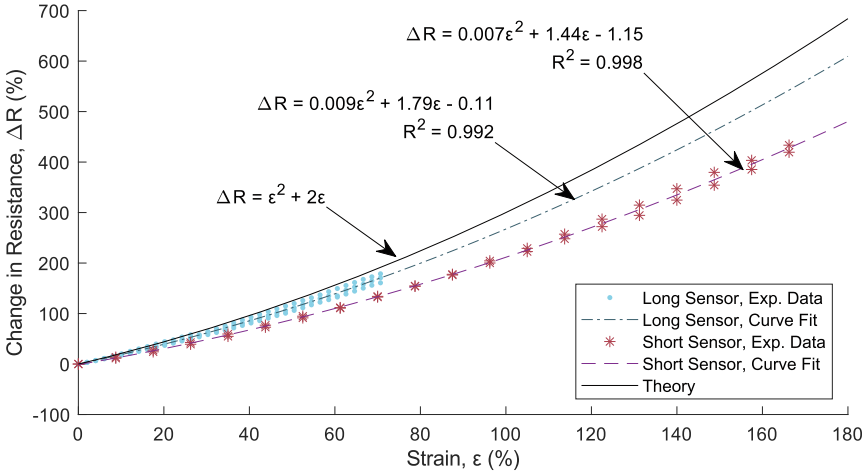

Fig. 4. Resistance response of two strain gauges with different lengths. The "Long" sensor measured 495.3 mm long and was extended up to 350 mm, corresponding to a strain of ∼71%. The "Short" sensor measured 114.3 mm long and was extended up to 200 mm, corresponding to a strain of ∼175%. The calculated theoretical resistance assumes a quadratic relationship between strain and resistance. Discrepancies between the experimental and theoretical results could be due to electrical contact resistance between the conductive fluid and the hypodermic tubing used in the sensor.

Due to limitations in the maximum travel speed of the MTS crosshead, the strain gauges did not experience the full range of cyclical motion for the higher cycling frequencies of 0.25 Hz and 0.13 Hz (Fig. 5b). As testing progressed from higher to lower cycling frequencies, the strain sensor visually exhibited slack when the crosshead returned to 0 mm extension between frequencies. The slack is evident in the data by examining the strains corresponding to 0 kPa stress. The strain gauge experienced 0 kPa stress at progressively higher strain values after each sequentially tested frequency.

3.3 Electromechanical Hysteresis

The strain gauge exhibited low electromechanical hysteresis, demonstrated by plotting the strain-strain response from both the strain gauge and video footage of the actuator (Fig. 6). The relationship is mostly linear with $R^2 = 0.993$ when evaluated using $y = x$. There is no distinct hysteresis loop visible in the figure. The strain calculated from the sensor signal deviates from the linear relationship between approximately 10% to 30% video data strain, with a peak mean deviation of 2.1% sensor signal strain at 20.6% video data strain.

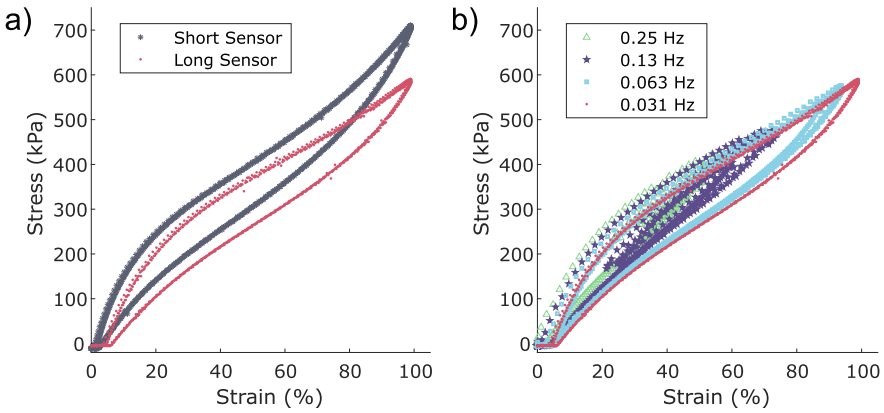

Fig. 5. Stress-strain hysteresis loops of strain gauges when cycled on a material testing system up to 100% strain. a) Both lengths of strain gauges exhibited similar hysteresis loops when cycled at a frequency of 0.031 Hz. The shorter, 114.3 mm-long sensor showed a higher peak stress than the longer, 495.3 mm-long sensor. b) Due to limitations of the testing system's crosshead speed, the strain gauges did not reach the full range of motion at higher frequencies of 0.25 Hz and 0.13 Hz. As the testing progressed from higher to lower frequencies, a 495.3 mm-long sensor's hysteresis loop shifted to the right, and the zero-stress crossing point corresponded to increasingly higher strain values, which suggests plastic deformation within the strain gauge.

3.4 Contact Detection

The strain sensor signal from the contact detection experiment shows a 1.00 V peak difference between the sensor data with and without contact (Fig. 7). The data presented were averaged over 5 cycles, using the 0 kPa pressure setpoint signal as a synchronizing reference. The peak pressure setpoint of 69 kPa was reached between 4–5 s, as expected from the 0.13 Hz pressure signal frequency. Due to the amplified Wheatstone bridge, an increase in resistance corresponds to a decrease in signal voltage. The sensor data without contact shows a minimum value of 1.37 V, corresponding to the highest inflation pressure in the actuator and the highest strain experienced by the strain gauge during contactless data collection. In contrast, the strain sensor voltage drops to a value of 0.37 V after contacting the ball, which is the saturation voltage of the signal amplifier and corresponds to a higher strain gauge resistance than in the contactless data.

4 Discussion

The strain sensor exhibits a resistance-strain response that follows a second-order curve fit, as expected by Eq. 5. We note that the fitted curves for both the 495.3 mm-long and 114.3 mm-long sensors lie below the quadratic relationship expected from theory (Fig. 4). This could be due to additional fixed-value

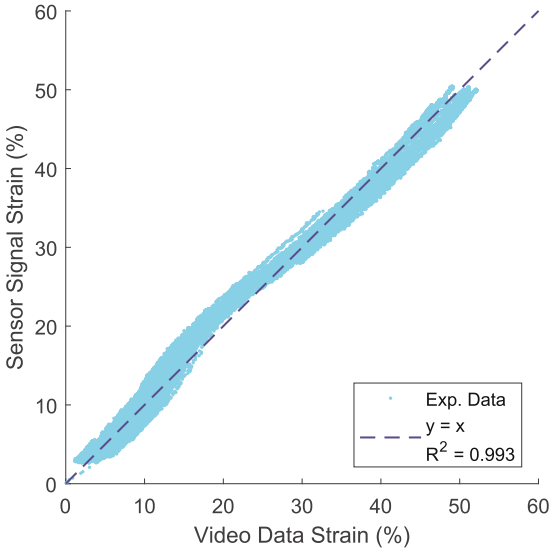

Fig. 6. The strain sensor did not exhibit noticeable strain-strain hysteresis when mounted on an actuator and cycled at varying frequencies. This suggests that any hysteresis in the integrated actuator-sensor system is dominated by the viscoelastic response of the McKibben actuator rather than by the sensor. In addition, the strain response measured by the sensor was nearly 1:1, with the strain calculated by a video imaging method. As a result, the strain gauge can be considered to provide quick and accurate feedback for sensing the state of the McKibben actuator. Discrepancies around 20–30% strain may be due to nonlinear effects of the McKibben actuator's geometry that require additional modeling when processing the video image data.

resistances within the strain gauge, such as contact resistances and the resistance of the stainless steel tubing, that were not a function of strain and were not modeled. The strain gauge resistance is composed of both fixed and strain-varying resistances. In an extreme, hypothetical case where the strain gauge was constructed from materials that do not exhibit any strain-varying resistance, we would expect to see a flat line with respect to strain. As the proportion of strain-varying resistance increases relative to fixed resistance, we expect the strain gauge's resistance-strain response to approach the curve described by Eq. 5. Supporting this hypothesis, we found that the longer 495.3 mm-long sensors are in closer proximity to the theoretical curve than the shorter 114.3 mm-long sensors. The longer sensors contain a greater proportion of elastomer tubing and conductive fluid than the shorter sensors and, therefore, a higher proportion of strain-varying to fixed resistance.

Regarding contact resistances within the strain gauge, we noted that the initial sensor resistance tended to be higher than expected immediately after fabrication, by up to multiple ohms. This discrepancy was rectified to the milliohm range by rapidly stretching and releasing the strain sensor. We hypothesize

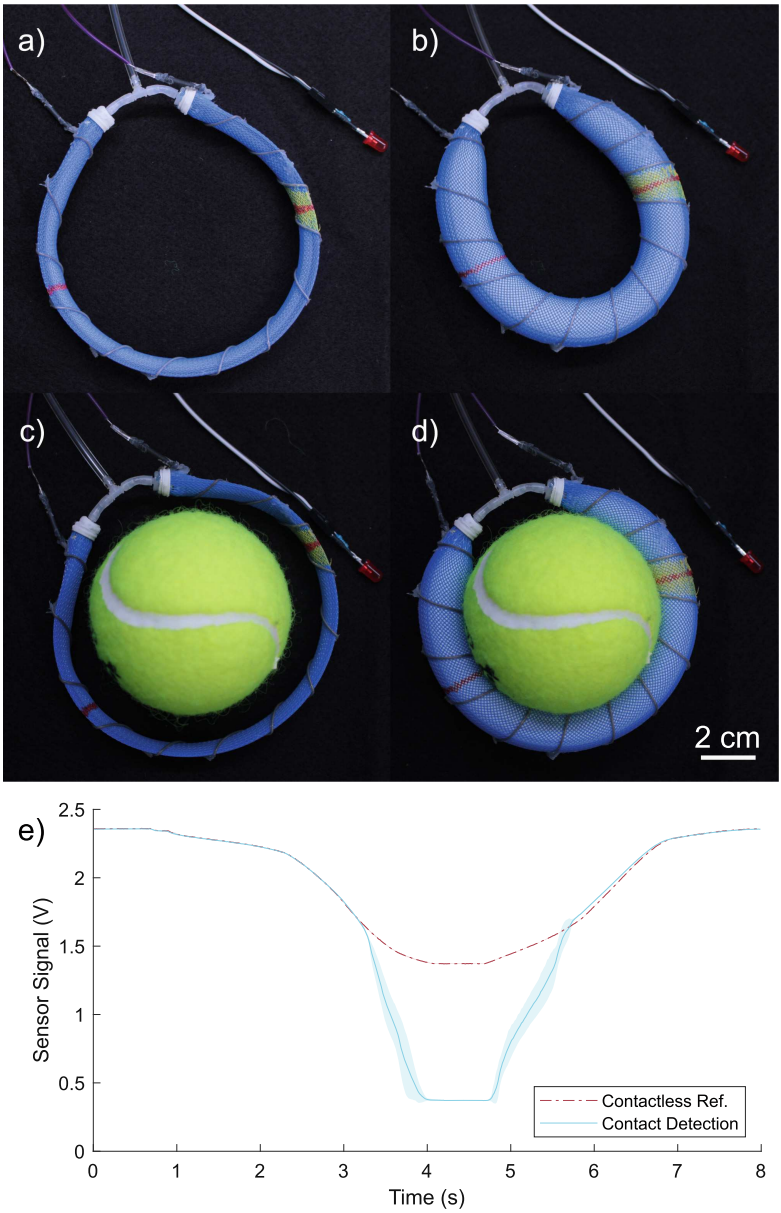

Fig. 7. The strain sensor was evaluated for contact detection capability by monitoring the sensor signal with and without contact. Contactless data was collected as the actuator was cycled between the a) deflated and b) inflated states while no object was present. Contact detection data was collected after c) placing a tennis ball within the actuator's circumference and d) pressurizing the actuator. e) The contact is observable through a sudden drop in the strain sensor's voltage signal. Lines indicate mean values, while shaded regions represent standard deviation.

that the high initial resistance could result from poor surface wetting between the EGaIn and the stainless steel hypodermic tubing. Surface wetting may have been improved by applying high acceleration to perturb the liquid within the strain sensor. In addition, gallium is known to form an oxide layer that can increase interfacial contact resistance [13]. In the future, hydrochloric acid vapor treatment could be explored during strain gauge fabrication to eliminate the oxide layer and reduce contact resistance.

The tested strain gauges exhibited mechanical stress-strain hysteresis as expected from their elastomer components. The non-Hookean stress-strain curves, with softening at intermediate strain values, are representative of the Mullins effect in viscoelastic materials [12]. When cycled at 0.031 Hz, the different peak stresses for the different lengths of strain gauges could be due to a combination of the Mullins effect and the different clamping methods used for each sensor length. As elastomers are exposed to higher peak strains and stresses, they will become softer at lower strain values. We note that the long sensor was softer than the short sensor at high strain values, which could be explained if the long sensor had experienced higher peak stress in prior testing. Since the longer strain gauges were formed into a U-shape for clamping into the material testing system, there was a portion of the strain gauge that was wrapped 180° around a 10 mm-diameter magnet. This wrapped portion of the strain gauge may have led to effective shortening of the strain sensor and, consequently, higher stresses or strains than expected for a given extension length. Slack that developed within the strain gauge during testing was likely due to plastic deformation. In the future, robotic applications that experience high strain should consider conditioning the sensor beforehand by stretching the sensor to high strain prior to any signal calibration.

The strains calculated from the sensor's voltage signal demonstrated a nearly linear relationship with the strain calculated from video footage of the actuator, suggesting a low amount of electromechanical hysteresis. Hysteresis is characterized by time-dependent variations between independent and dependent variables that would result in loops in the plotted data. The lack of an obvious hysteresis loop indicates little to no time shift between the sensor's physical strain and voltage signal. As a result, any hysteresis in the sensorized McKibben actuator would likely be due to mechanical viscoelastic effects in the McKibben actuator or the strain gauge, as opposed to electromechanical hysteresis in the sensor signal. Low electromechanical hysteresis sensors are important for accurate sensing, as the strain gauge's signal will respond quickly to changes in strain.

The bump in the strain-strain curve around 20.6% video data strain could be a result of modeling errors, such as when establishing the relationship between h and t (Fig. 3). We note that there is a nonlinear response in the actuator's cross-section dimensions with respect to pressure, which is indicated by the uneven intervals between collected data. While a second-order curve was fit to the data, future collection of cross-sectional dimensions at a higher resolution in t could result in a different fit, such as a piecewise linear function with a knee around $t =$ 10.4 mm. We note that the scaling of the strain-strain relationship was sensitive

to the assumptions made when post-processing the video data due to the effects of the assumptions on the strain gauge's calculated initial length. However, the assumptions did not affect trends in the data. We made no time-dependent assumptions that would result in a hysteresis loop if inaccurate.

During contact detection experiments, contact between the sensor and the tennis ball resulted in an abrupt change in sensor signal voltage as compared to the contactless signal data. As mentioned previously, the signal voltage decreases when the sensor resistance increases, due to the signal amplifier circuit. When the actuator and strain gauge touched the tennis ball, the ball pressed on the strain sensor's elastomer tubing and reduced the cross-sectional area of conductive fluid, resulting in higher resistance. The rapidly increased resistance during contact is responsible for the sudden drop in sensor signal voltage. The large 1.00 V contrast in signal voltage is desirable to distinguish contact events from false positives if used as a digital signal. Further experimentation to relate contact force and signal voltage could also enable high-resolution analog force sensing.

Integrating strain sensing with soft pneumatic actuators can provide additional sensing modalities for improved functionality in soft robots. In robots that solely monitor actuator pressure, state control may rely on open-loop control with predefined models that cannot robustly respond to disturbances. The addition of strain sensing as a second modality can help close the loop for robust control of pose with respect to both the robot and the external environment. Beyond measuring strain directly, strain sensors with contact detection capabilities can be used for proprioception between internal components, for orientation to environmental landmarks, and for applications including grasping and manipulation. The presented work demonstrates an easily fabricated strain gauge that can be used as a contact detection sensor to support these applications in the future. Since the strain gauge can be fabricated asynchronously from the fluidic actuator and without direct integration in the actuator's elastomer components, fatigue failures of elastomer elements can be easily repaired at low cost.

Further developments to the presented strain sensor will focus on reducing the contact resistance between the conductive fluid and the stainless steel leads or explore alternative materials for fabrication. In addition, characterizing the sensor's electromechanical hysteresis using automated data collection methods may help further quantify the sensor's signal response speed. We would also like to explore the integration of these sensors into an increased variety of actuators for internal proprioception in soft robots. As soft robots incorporate greater varieties of actuators, model-free integration of these sensors into robotic applications may become desirable to eliminate the sensor modeling and assumptions made in this paper.

5 Conclusion

The presented strain sensor design provides a possible solution for integrating strain sensing into existing soft robotic actuators. The simple manufacturing

process of the strain gauge can enable rapid series production of several sensors. Characterization of these sensors showed expected resistance-strain and stress-strain responses when compared to engineering models. The low electromechanical hysteresis of these sensors suggests a sufficiently high response rate to changes in strain when mounted on a cyclically pressurized McKibben actuator. In addition to detecting changes in length, the sensor also displayed a high-contrast electrical signal for detecting contact between an actuator and a gripped ball. Further development of the sensor could provide a low-cost sensing solution for applications in soft robotic proprioception and manipulation.

Acknowledgements. The authors would like to thank Ashlee Liao for insightful feedback during manuscript editing.

References

1. Analog Devices: Single and Dual-Supply, Rail-to-Rail, Low Cost Instrumentation Amplifier, September 2020. rev. G
2. Cooper, C.B., et al.: Stretchable capacitive sensors of torsion, strain, and touch using double helix liquid metal fibers. Adv. Funct. Mater. **27**(20), 1605630 (2017). https://doi.org/10.1002/adfm.201605630
3. Dai, K., et al.: SLUGBOT, an aplysia-inspired robotic grasper for studying control. In: Biomimetic and Biohybrid Systems. Living Machines 2022. LNCS, vol. 13548, pp. 182–194. Springer, Cham (2022). https://doi.org/10.1007/978-3-031-20470-8_19
4. El-Atab, N., et al.: Soft actuators for soft robotic applications: a review. Adv. Intell. Syst. **2**(10), 2000128 (2020). https://doi.org/10.1002/aisy.202000128
5. Huang, X., et al.: Chasing biomimetic locomotion speeds: creating untethered soft robots with shape memory alloy actuators. Sci. Robot. **3**(25), eaau7557 (2018). https://doi.org/10.1126/scirobotics.aau7557
6. Kanno, R., Watanabe, S., Shimizu, K., Shintake, J.: Self-sensing McKibben artificial muscles embedded with dielectric elastomer sensor. IEEE Robot. Autom. Lett. **6**(4), 6274–6280 (2021). https://doi.org/10.1109/LRA.2021.3093276
7. Kellaris, N., Gopaluni Venkata, V., Smith, G.M., Mitchell, S.K., Keplinger, C.: Peano-hasel actuators: muscle-mimetic, electrohydraulic transducers that linearly contract on activation. Sci. Robot. **3**(14), eaar3276 (2018). https://doi.org/10.1126/scirobotics.aar3276
8. King, J.P., Valle, L.E., Pol, N., Park, Y.L.: Design, modeling, and control of pneumatic artificial muscles with integrated soft sensing. In: 2017 IEEE International Conference on Robotics and Automation (ICRA), pp. 4985–4990. IEEE (2017). https://doi.org/10.1109/ICRA.2017.7989580
9. Klute, G.K., Hannaford, B.: Fatigue characteristics of McKibben artificial muscle actuators. In: Proceedings. 1998 IEEE/RSJ International Conference on Intelligent Robots and Systems. Innovations in Theory, Practice and Applications (Cat. No. 98CH36190), vol. 3, pp. 1776–1781. IEEE (1998). https://doi.org/10.1109/IROS.1998.724854
10. Kothera, C.S., Jangid, M., Sirohi, J., Wereley, N.M.: Experimental characterization and static modeling of McKibben actuators. J. Mech. Des. **131**(9) (2009). https://doi.org/10.1115/1.3158982

11. Majidi, C.: Soft-matter engineering for soft robotics. Adv. Mater. Technol. **4**(2), 1800477 (2019). https://doi.org/10.1002/admt.201800477
12. Ogden, R.W., Roxburgh, D.G.: A pseudo-elastic model for the mullins effect in filled rubber. Proc. R. Soc. Lond. Ser. A Math. Phys. Eng. Sci. **455**(1988), 2861–2877 (1999). https://doi.org/10.1098/rspa.1999.0431
13. Ozutemiz, K.B., Wissman, J., Ozdoganlar, O.B., Majidi, C.: EGain-metal interfacing for liquid metal circuitry and microelectronics integration. Adv. Mater. Interfaces **5**(10), 1701596 (2018). https://doi.org/10.1002/admi.201701596
14. Piazza, A., Parker, A.: Highly elastic strain gage for low modulus materials. In: 2015 WRSGC Winter Test and Measurement Meeting. No. DFRC-E-DAA-TN22087 (2015)
15. Tondu, B.: Modelling of the McKibben artificial muscle: a review. J. Intell. Mater. Syst. Struct. **23**(3), 225–253 (2012). https://doi.org/10.1177/1045389X11435435
16. Wirekoh, J., Valle, L., Pol, N., Park, Y.L.: Sensorized, flat, pneumatic artificial muscle embedded with biomimetic microfluidic sensors for proprioceptive feedback. Soft Robot. **6**(6), 768–777 (2019). https://doi.org/10.1089/soro.2018.0110
17. Zhong, S., et al.: A contraction length feedback method for the McKibben pneumatic artificial muscle. Sens. Actuators A **334**, 113321 (2022). https://doi.org/10.1016/j.sna.2021.113321
18. Zhu, S., et al.: Ultrastretchable fibers with metallic conductivity using a liquid metal alloy core. Adv. Funct. Mater. **23**(18), 2308–2314 (2013). https://doi.org/10.1002/adfm.201202405